Discovering cryptic pocket opening and binding of a stimulant derivative in a vestibular site of the 5-HT$_{3A}$ receptor

Nandan Haloi[1], Emelia Karlsson[2], Marc Delarue[3,4], Rebecca J. Howard[1,2*], Erik Lindahl[1,2*]

[1]Department of Applied Physics, Science for Life Laboratory, KTH Royal Institute of Technology, Tomtebodavägen 23, Solna, SE-17165, Sweden.
[2]Department of Biochemistry and Biophysics, Science for Life Laboratory, Stockholm University, Tomtebodavägen 23, Solna, SE-17165, Sweden.
[3]Unité Dynamique Structurale des Macromolécules, Institut Pasteur, 25 Rue du Docteur Roux, FR-75015, Paris, France.
[4]Centre National de la Recherche Scientifique, CNRS UMR3528, Biologie Structurale des Processus Cellulaires et Maladies Infectieuses, 25 Rue du Docteur Roux, FR-75015, Paris, France.

*Corresponding author(s). E-mail(s): rebecca.howard@dbb.su.se; erik.lindahl@dbb.su.se;

Abstract

Ligand-gated ion channels propagate electrochemical signals in the nervous system. A diverse set of allosteric modulators including stimulants, anesthetics, and lipids regulate their function; however, structures of ligand-bound complexes can be difficult to capture by experimental methods, particularly when binding is dynamic or transient. Here, we used computational methods and electrophysiology to identify a possible bound state of a modulatory stimulant derivative in a cryptic vestibular pocket of a mammalian serotonin-3A receptor. Starting from a closed-pocket experimental structure, we first applied a molecular dynamics simulations-based goal-oriented adaptive sampling method to identify possible open-pocket conformations. To find plausible ligand-binding poses, we performed Boltzmann docking, which combines traditional docking with Markov state modeling, of the newly sampled conformations. Clustering and analysis of stability and accessibility of docked poses supported a preferred binding site; we further

validated this site by mutagenesis and electrophysiology, suggesting a mechanism of potentiation by stabilizing intersubunit contacts. Given the pharmaceutical relevance of serotonin-3 receptors in emesis, psychiatric and gastrointestinal diseases, characterizing relatively unexplored modulatory sites such as these could open valuable avenues to understanding conformational cycling and designing state-dependent drugs.

Keywords: cryptic pocket, vestibular site, ligand-gated ion channel, adaptive sampling, MD simulations, electrophysiology

Introduction

Pentameric ligand-gated ion channels (pLGICs) play a central role in intercellular communication in the mammalian nervous system [1]. In a classical example, neurotransmitters released at the synaptic cleft bind to corresponding pLGICs, contracting the extracellular domain (ECD) and opening a permeation pore in the transmembrane domain (TMD) to allow ions to cross the membrane for further signal transduction [2] (Fig. 1A). A diverse set of ligands, including anesthetics, neurosteroids, and lipids, can modulate these proteins via orthosteric or various binding sites. For example, in serotonin-3 receptors (5-HT_3Rs), antiemetic drugs such as palonosetron, used in the treatment of nausea and vomiting associated with radiation and chemotherapies, compete with serotonin binding at the orthosteric site to inhibit channel function [3]. Conversely, in type-A γ-aminobutyric acid receptors ($GABA_A$Rs), classical benzodiazepine drugs that are used to treat epilepsy, anxiety, and insomnia bind allosteric sites distinct from GABA binding to modulate neurotransmitter activation [4–6].

Whereas both the orthosteric neurotransmitter site and ECD benzodiazepine site are located at extracellular subunit interfaces (Fig. 1A), the ECD interior vestibule constitutes a relatively unexplored allosteric ligand-binding site (Fig. 1B). Several X-ray structures of prokaryotic pLGICs contain ligands in this region, including the benzodiazepine flurazepam in the plant-pathogen channel ELIC (Fig. 1C) [7], and various modulatory carboxylates in the proton-gated channel GLIC (Fig. S1) [8–10]. The channel sTeLIC, derived from an endosymbiont of the tubeworm *Tevnia jerichonana*, was recently crystallized with the positive modulator 4-bromocinnamate in its vestibule [11] (Fig. 1C). In these cases, ligands were identified in each subunit between the β4, β5, and β6 strands, in a cavity defined by the so-called Ω-loop (Fig. 1B–C).

A role for the ECD vestibule in ligand binding and modulation of eukaryotic pLGICs is less clear. As demonstrated by Brams and colleagues [12], this cavity is occluded in experimental structures of most eukaryotic pLGICs, including α2/3 nicotinic acetylcholine receptor subunits [13, 14] and α1/3 glycine receptor subunits [15]. The vestibular cavity appears to be more accessible in 5-HT_{3A}Rs [16]; indeed, cysteine-scanning mutagenesis of human 5-HT_{3A}Rs indicated this region to be sensitive to modulation by covalent labeling [12]. However, the 5-HT_{3A}R Ω-loop is not conserved with that of prokaryotic channels known to bind vestibular ligands (Fig. 1C), and direct evidence for drug modulation via this region in a eukaryotic system remains lacking.

Molecular dynamics (MD)-based techniques offer complementary approaches to explore binding sites not readily apparent in experimental structures [17–20]. Here, we applied a goal-oriented adaptive sampling method [21] to explore regions of conformational space relevant to the opening of a potential binding pocket in the ECD vestibule of a mammalian 5-HT_{3A}R. Then, to find plausible ligand-binding poses, we performed ensemble docking of 4-bromoamphetamine resulting in a total of 1.5 million docked poses, and reweighted docking scores by the Boltzmann energy function derived from Markov state model analysis of our trajectories. Following clustering of the top 100 docked poses, we then performed replicate unbiased MD simulations of representative complexes in two forcefields to estimate ligand stability, and screened the most stable complexes for accessibility to the aqueous environment. For one relatively

stable and accessible site, mutations predicted to disrupt 4-bromoamphetamine binding and/or modulation were validated by our electrophysiology recordings in *Xenopus laevis* oocytes, and provided a mechanistic rationale for the allosteric stabilization of an activated state.

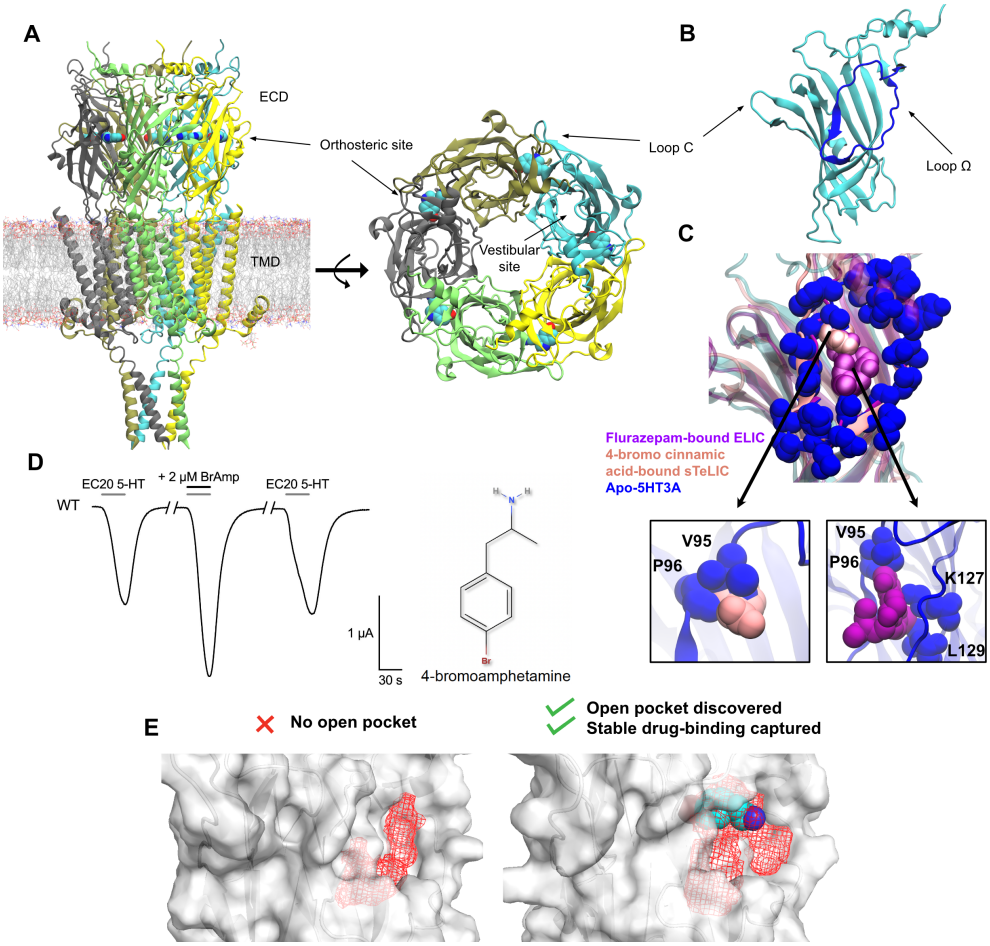

Fig. 1 Overview of 5-HT$_{3A}$R structure and pharmacology explored in this work. A) Architecture of a representative 5-HT$_{3A}$R, colored by subunit, viewed from the membrane plane (left) and from the extracellular side (right). Serotonin bound at the orthosteric site is represented in van der Waals spheres. B) ECD of a single 5-HT$_{3A}$R subunit, with the Ω-loop in blue. C) Structural alignment of putative vestibular sites in ELIC (PDB ID: 2YOE, purple), sTeLIC (PDB ID: 6FLI, pink), and the 5-HT$_{3A}$R (PDB ID: 6DG8, blue). In ELIC and sTeLIC, spheres represent vestibule-bound ligands flurazepam and 4-bromocinnamate, respectively. In the 5-HT$_{3A}$R, spheres represent amino-acid side chains in the Ω-loop. Insets show steric clash of ligands in sTeLIC (left) and ELIC (right) with the 5-HT$_{3A}$R Ω-loop, indicating an occluded pocket. D) Representative current trace from a 5-HT$_{3A}$R-expressing *Xenopus* oocyte in the absence and presence of 4-bromoamphetamine during serotonin pulses. E) Pocket volumes at the 5-HT$_{3A}$R vestibular site, generated in Fpocket [22], show a superficial cavity in the experimental structure (*left*), but a clearly opened pocket surrounding the docked pose of 4-bromoamphetamine (*right*), as found in our study. Pocket volumes are shown in red mesh, the ligand in van der Waals, and the receptor in gray surface representations.

Results

Lack of structural rationale for 4-bromoamphetamine modulation in experimental data

In exploring potential vestibular pLGIC modulators, we noted that a ligand previously crystallized in the vestibule of the prokaryotic channel sTeLIC, 4-bromocinnamate [11], is structurally similar to amphetamine psychostimulants. Interestingly, the closely related compound 4-bromoamphetamine enhanced serotonin-stimulated currents through 5-HT_{3A}Rs at low micromolar concentrations in *Xenopus* oocytes (Fig. 1D). However, we found that the Ω-loop in experimental 5-HT_{3A}R structures was generally contracted compared to prokaryotic homologs, even in an activated state presumed to be stabilized by positive allosteric modulators (PDB IDs 6DG8 and 4PIR) [12, 23]. Solvent-accessible volume in this pocket was limited (Fig. 1E, Fig. S2): although smaller dicarboxylates could fit (based on structural alignment with GLIC structures (Fig. S1), ligands on the scale of 4-bromoamphetamine or larger (such as 4-bromocinnamate and flurazepam) superimposed from complexes with sTeLIC and ELIC, respectively, clashed with 5-HT_{3A}R Ω-loop sidechains (Fig. 1C).

To more thoroughly investigate potential binding in this site, we performed molecular docking around the Ω-loop of an activated 5-HT_{3A}R structure, and subjected this complex to unrestrained MD simulations. The modulator deviated rapidly (within 20 ns) and dramatically (>15 Å root-mean-square deviation, RMSD) from the docked pose, and sampled increasingly distant poses over time (Fig. S3). If the 5-HT_{3A}R vestibule does mediate 4-bromoamphetamine modulation, it would appear to involve a cryptic pocket, i.e. a binding site that is intrinsically transient or otherwise not readily apparent in experimental structures [17]. We also ran 25 replicate unrestrained simulations in the absence of modulator, but observed limited flexibility in the Ω-loop (root-mean-square fluctuation $<$ 1.8 Å, Fig. S4) relative to other regions, indicating that enhanced sampling methods would be required to capture an alternative open state of this putative binding site.

An adaptive sampling and docking-based workflow to capture a stable, accessible ligand site

We next applied an adaptive sampling method, fluctuation amplification of specific traits (FAST) [21], to launch simulations from the closed-pocket 5-HT_{3A}R structure and maximize the chance of discovering cryptic pockets that may harbor new ligand binding sites (see Methods for details) (Fig. 2A). Within 30 simulation generations, we observed an increase in pairwise distances between residues in the Ω-loop and neighboring β-strand walls, associated with a widening of the Ω-loop as well as more modest increases in pocket volume and solvent-accessible surface area (Fig. 2A, Fig. S5).

To capture ligand binding to these newly explored conformations, we next performed ensemble docking of 4-bromoamphetamine to all FAST-sampled MD trajectories, a total of 30 μs simulations (Fig. 2B). Although a docking score can indicate the likelihood of binding a particular pocket conformation, its potential contribution will be much less if the conformation itself is not thermodynamically stable. Hence,

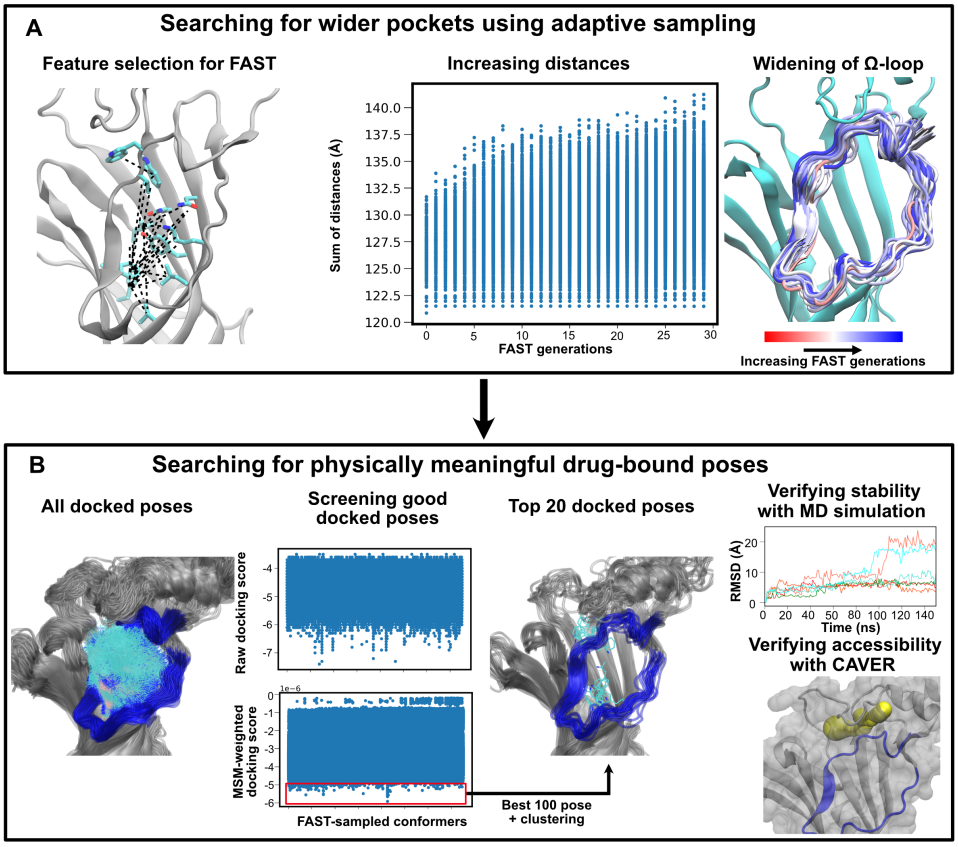

Fig. 2 A two-phase computational workflow developed in this study to model first pocket opening and then ligand binding. A) Left: in FAST sampling, starting points for successive generations were selected on the basis of pairwise distances (dashed lines) between residues (cyan) in the Ω-loop and neighboring β-strands. Center: these distances increased in successive FAST generations, each containing 1 μs of MD simulations data. Right: FAST sampling was also associated with progressive widening of the Ω-loop, as depicted by representative snapshots colored by generation (red to blue). B) Left: FAST-generated conformers were subjected to molecular docking with 4-bromoamphetamine. Center: docked scores were then re-weighted by the stationary probability of the corresponding protein conformation, determined by Markov state model analysis. The 100 best poses (red box) were then clustered based on RMSD of the ligand atoms with a cutoff of 2.5 Å, and screened down to 20 representative poses. Right: these poses were then used for further MD simulations and accessibility analysis.

we re-weighted the docking scores according to the equilibrium probability of the corresponding protein conformations based on a Markov state model of the FAST-sampled trajectories (Fig. 2B). This approach, termed Boltzmann docking, has been shown to improve activity predictions for small molecules in targets such as TEM β-lactamase [24].

From the 100 best Boltzmann-docked 4-bromoamphetamine complexes, we reduced redundancy using RMSD-based clustering, resulting in twenty representative putative

poses (Fig. 2B). We then tested their stability by performing unbiased MD simulations. Since small-molecule parameters can be sensitive to the choice of forcefields, we performed three replicate simulations of each system in both CHARMM36m [25–28] and AMBER [29, 30], for a total of 20 systems x 3 replicates x 2 forcefields = 120 150-ns trajectories (Fig. S7).

For closer analysis, we selected systems in which the ligand remained relatively stable (<15 Å center-of-mass RMSD) throughout at least 5 of its 6 replicate simulations. In the six systems that passed this filtering (Fig. S7), we further analyzed the contact frequency of the ligand with each receptor residue. Interestingly, one of these systems (pose 20) positioned the ligand between the β2, β4 and β6 strands (site 1, Fig. 3A–B), similar to the 4-bromocinnamate site in sTeLIC (Fig. 1C). In the remaining five relatively stable systems (poses 8, 12, 13, 16, 18), the ligand occupied a distinct region (site 2, Fig. 3B–C) defined by the β1, β2, β4, and β8 strands. Notably, the RMSD of the ligand in site 1 was moderately higher (around 5 Å, Fig. 3B) because during simulations the initial docked pose slightly adjusted its orientation, converging to the end pose seen in Fig. 3A.

Although even more stable than site 1, poses in site 2 were buried in an enclosed cavity, substantially shielded from solvent by the outermost ECD (Fig. 3B-C). We noted that computational docking and simulations might retain a ligand in a pocket entirely inaccessible from the solvent, rendering binding physically implausible. Therefore, we also analyzed the accessibility of both putative sites using the CAVER software suit [31] (Fig. 2B). In site 1, the ligand amino group was directly exposed to solvent, with the pocket clearly accessible to the aqueous medium (Fig. 3D). However, in site 2, accessibility analysis showed no pathways for ligand entry (Fig. 3E). Accordingly, we proceeded to focus on site 1 as a physically plausible region for ligand binding and modulation.

Structural features and functional validation of a vestibular modulatory site

The putative 5-HT$_{3A}$R vestibular site contained several hydrophobic residues (β2-W68, β4-W94, β6-V123) lining the inner wall, making van der Waals contacts with the bromine and aromatic groups of the ligand (Fig. 3A–B). The mouth of the putative site contained more polar residues (β2-Q66, β3-T90, β6-N125), interacting with the ligand amino group. In comparing the experimental structure to the putative bound state derived from our simulations, the most dramatic change in the Ω-loop was an outward shift and rotation of the β4 strand, relieving prospective clashes of the ligand with residues β4-V95 and -P96 (Fig. 1C, Fig. 4A). Local resolution is relatively poor in this region of β4 in multiple activated 5-HT$_{3A}$R cryo-EM structures (Fig. S9), indicating it could sample such alternative conformations. Interestingly, this transition moved V95 roughly 4 Å towards the subunit interface, bringing it into direct contact with residue P113 on β5 of the complementary subunit (Fig. 4A, C). A similar motion was previously reported for β4-F103, located at the bottom of the Ω-loop, out of the vestibule to interact with β6-P128 on the complementary subunit in open versus closed cryo-EM structures [32]. These effects are consistent with the general contraction of

the upper ECD associated with pLGIC activation [2], suggesting a mechanism for receptor potentiation via the vestibular site.

To functionally validate our putative ligand complex, we first engineered mutations at V95 and N125, two of the most frequent amino-acid contacts in simulations of this ligand pose (Fig. 4A–B). Substituting alanine at either of these positions weakened apparent serotonin sensitivity, increasing the agonist EC_{50} roughly 2-fold in 5-HT_{3A}R expressing oocytes (Fig. 4D). Moreover, at serotonin concentrations giving equivalent levels of activation, either substitution significantly reduced potentiation by 600 nM–6 μM 4-bromoamphetamine, rendering the receptor largely insensitive to the modulator (Fig. 4E). We further hypothesized that drug displacement of V95 towards P113 in the complementary subunit would promote interfacial contraction, thereby facilitating channel activation (Fig. 4A, C). In support of this model, substituting glycine at P113 dramatically suppressed potentiation by 4-bromoamphetamine, similar to its direct contacts in the vestibular site (Fig. 4E). Thus, functional recordings of site-directed mutants were in agreement with computational measurements of stability and accessibility in predicting a vestibular potentiating mechanism in the 5-HT_{3A}R.

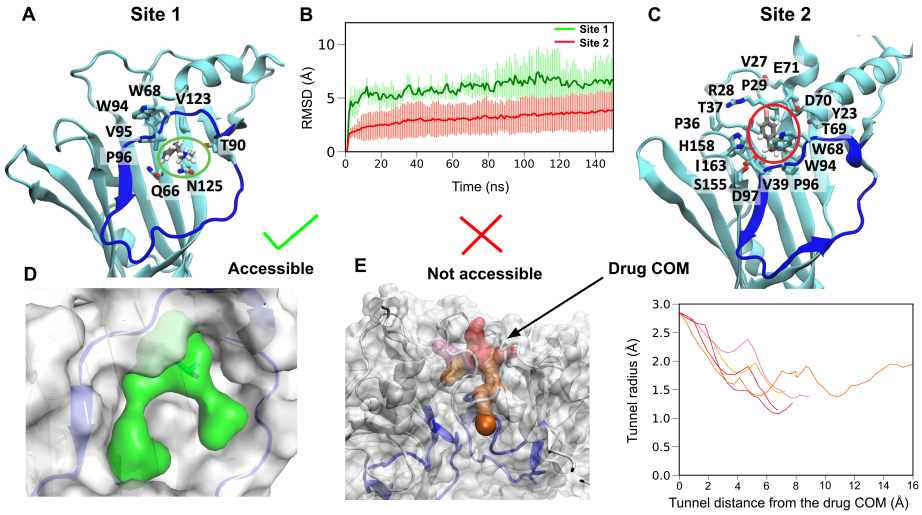

Fig. 3 Comparison of stable sites captured by MD simulations of Boltzmann docked poses. A) Interacting residues (cyan, >50 % contact probability in MD simulations) surrounding the ligand (gray) in site 1. For clarity, hydrogens are hidden in protein side chains, and the Ω-loop backbone is shown in blue. B) Ligand stability in sites 1 (green) and 2 (red), as represented by RMSD of 4-bromoamphetamine from its initial docked pose during MD simulations, averaged across all stable replicates. Shaded regions indicate standard deviations. C) Interacting residues surrounding the ligand in site 2, depicted as in *A*. D) Based on accessibility analysis in CAVER [31], the ligand pocket (green) in site 1 is clearly accessible to solvent. E) In site 2, molecular representations (left) and radius plots (right) show no open accessible pathways (shades of red) to the ligand center of mass.

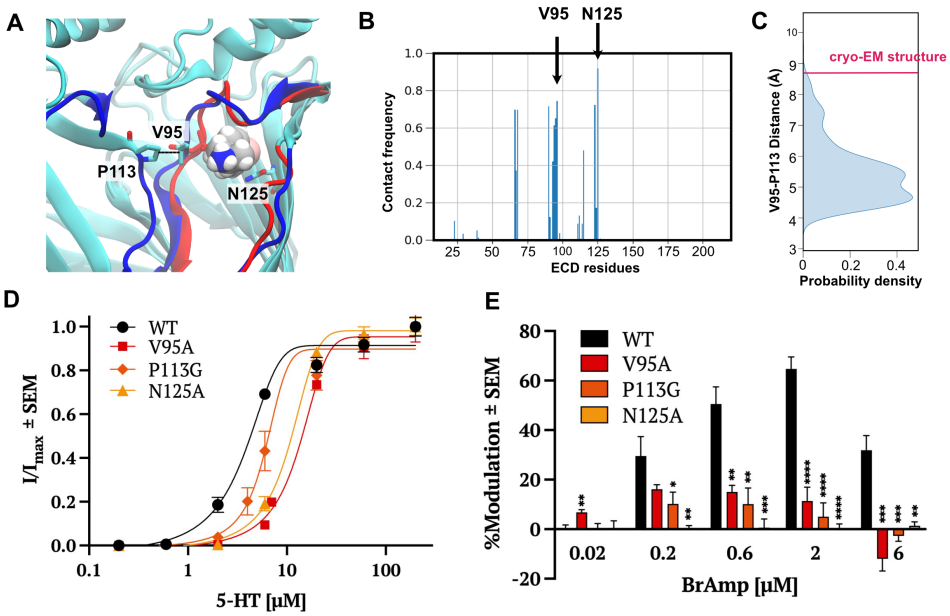

Fig. 4 Structural features and functional validation of a vestibular modulatory site. A) Remodeling of the $\beta 4$-strand in open- (blue) versus closed-pocket models (red) of the 5-HT$_{3A}$R enables stable binding of the ligand (gray spheres) between residues V95 and N125, and positions V95 in proximity to P113 on the complementary subunit. For clarity, amino-acid side chains are shown as cyan sticks without hydrogens. B) Frequency of contacts between 4-bromoamphetamine in site 1 and individual residues of the 5-HT$_{3A}$R ECD in MD simulations. A contact is counted if two atoms of the ligand and receptor are within 4 Å of one another. C) Probability distribution of the minimum distance between the side-chain atoms of V95 and P113 on neighboring subunits, calculated over all stable MD simulation replicates associated with site 1. The distance captured in the cryo-EM structure (PDB ID: 6DG8) is highlighted red. D) Concentration-response curves for 5-HT activation of wild-type (WT) and mutant 5-HT$_{3A}$Rs expressed in *Xenopus* oocytes. E) Percent modulation of WT, V95A, N125A, and P113G 5-HT$_{3A}$R currents by 4-bromoamphetamine (n $\geq$ 5), relative to EC20 5-HT currents measured immediately before treatment. Asterisks indicate significance relative to WT (*P $\leq$ 0.05, **P $\leq$ 0.01, ***P $\leq$ 0.001, ****P $\leq$ 0.0001).

Discussion

The resolution revolution has increasingly enabled single-particle cryo-EM reconstructions of previously inaccessible systems, including complex membrane proteins such as pLGICs [33]. While these advances have the potential to launch a new era of structure-based drug design, relatively few structures have been determined in the presence of novel drugs. Visualizing drug binding at an atomic level, including the ligand and protein interactions and geometries, can support the design of pharmaceuticals that mimic the chemical structure, binding mode, and functional effect of known modulators. A persistent challenge in the field is that binding pockets may not be readily apparent in unliganded structures, probably due to their transient nature. Therefore, to exploit the full potential of structural data, new types of methods are needed.

MD simulation and machine learning-based techniques offer notable opportunities to explore cryptic or otherwise experimentally obscure sites [17–20]. In MD simulations, a major challenge is the time scale required to transition a cryptic pocket from a closed to open state. Popular methods, in addition to FAST [21], include sampling water interfaces through scaled Hamiltonians (SWISH), in which nonbonded interactions of solvent molecules with protein atoms are progressively scaled, shifting the water properties toward more ligand-like behavior to promote cryptic-pocket opening [17]. A general challenge to MD-based methods is the need for computing resources and a system-specific simulation setup, particularly for larger protein complexes. To address this challenge, one recent study demonstrated the power of stochastic subsampling of multiple sequence alignment depth in AlphaFold2 combined with Markov state modeling to accelerate the discovery of novel cryptic pockets [19, 34]. Another study showed the effectiveness of training graph neural networks based on a large MD dataset to find cryptic pockets [18]. The FAST approach used here has been successfully applied to capturing pockets in Ebola viral protein 35 [35], SARS-CoV-2 [36] and the epidermal growth factor receptor [37], a notable diversity of targets.

Computational methods are inherently models offering predictions, and to confirm these predictions we have used electrophysiology functional assays. This work demonstrates a pipeline that was able to reveal a functionally validated vestibular binding of an amphetamine derivative in a eukaryotic pLGIC. Amphetamines are widely used to treat diseases such as attention deficit hyperactivity disorder, narcolepsy, and irritable bowel syndrome [38]. However, several adverse side effects such as anorexia, weight loss, insomnia, and dependence have been reported [38]. The amphetamine-5-HT_{3A}R complex proposed in this study could provide a starting point for designing analogous compounds to circumvent such side effects, especially given the structural conservation (presence of bromine in the same location in the aromatic ring with respect to the aliphatic amine) between the ligand investigated in this study, 4-bromoamphetamine, and a well-known psychoactive compound 2C-B ((4-bromo-2,5-dimethoxyphenethylamine)) [39]. It remains to be seen whether other eukaryotic channels such as glycine, acetylcholine, or $GABA_A$ receptors also contain modulatory sites in this region; application of our method to these systems could substantially enrich the development of pLGIC pharmacology.

Our results raise several mechanistic questions regarding vestibular modulation of 5-HT_{3A}Rs. Firstly, since we simulated pocket opening in the absence of a modulator,

our study cannot conclusively distinguish whether drug binding occurs via a conformational selection, induced fit, or combined mechanism. Metadynamics analysis could provide relevant insight, for instance by using our bound pose as a starting model and pocket opening/closing as well as drug binding/unbinding as reaction coordinates. Secondly, although our electrophysiology results showed that the ligand acts as a positive modulator, it remains unclear how ligand binding at the vestibular site may influence allosteric coupling between orthosteric serotonin binding and pore opening, especially since we mildly restrained the M2 helix of the TMD to prevent commonly observed pore-collapsing events of pLGICs in MD simulations [40]. The dynamic allosteric coupling could be investigated in principle using MD-based methods such as Markov state modeling or metadynamics, with our putative complex as a starting point and using polarizable forcefields that may better represent the hydration of the pore [41]. Given the evidence for cross-talk between the orthosteric and vestibular binding site in the bacterial channel GLIC [8–10], it would be interesting to see in the future if a similar trend can be found in 5-HT_{3A}R as well.

Overall, our results show how MD simulation-based methods can be used to sample previously unseen or cryptic binding pockets in cryo-EM structures and find stable drug binding that can be validated with experimental assays. This appears to be a promising approach both for sampling membrane protein binding pocket structural transitions in general, and in particular to identify novel modulatory binding sites in the 5-HT_{3A}R receptor and similar targets of high pharmaceutical relevance.

Methods

System preparations

Simulations were initiated from the serotonin-bound open-state cryo-EM structure of 5-HT_{3A} (PDB ID 6DG8) [23]. The structure was embedded a symmetric membrane that approximates neuronal plasma membrane composition [42]: 44.4% cholesterol, 22.2% 1-palmitoyl-2-oleoyl-sn-glycero-3-phosphocholine (POPC), 22.2% 1-palmitoyl-2-oleoyl-sn-glycero-3-phosphoethanolamine (POPE), 10% 1-palmitoyl-2-oleoyl-sn-glycero-3-phospho-L-serine (POPS) and 1.1% phosphatidylinositol 4,5-bisphosphate (PtdIns(4,5)P2). The system was built using the Membrane Builder module of CHARMM-GUI [43] by solvating with TIP3P water [44] and neutralizing in 0.15 M NaCl to generate systems containing 300,000 atoms, with dimensions of 130 $\times$ 130 $\times$ 200 $Å^3$. To allow for better sampling, 25 independent replicas were built by randomly configuring initial lipid placement around the protein using the Membrane mixer plugin in VMD [45, 46].

The systems were energy minimized and then relaxed in simulations at constant pressure (1 bar) and temperature (310K) for 30 ns, during which the position restraints on the protein and ligands were gradually released. The restraints were used as recommended by CHARMM-GUI. Then, production runs were performed with a mild position restraint of 50 kJ mol^{-1} nm^{-2} on the backbone atoms of the pore-facing residues at the M2 helix of the transmembrane domain (TMD), to prevent the commonly known pore-collapsing events of ligand-gated ion channels in MD simulations [40]. Since we are mainly interested in the sampling vestibular pocket at the extracellular domain (ECD), located around 45 Å away from the TMD, we reason that these restraints will not have any effect on our results. Also, a mild flat-bottom restraint of 20 kJ mol^{-1} nm^{-2} between the atoms of serotonin and residues at the binding sites was maintained, to prevent sudden release of GABA from the binding sites as been seen in our previous simulation.

Adaptive sampling

To explore possible pocket openings at the vestibular site, we applied a goal-oriented adaptive sampling method, called fluctuation amplification of specific traits (FAST) [21]. Briefly, the method runs successive swarms of simulations where the starting points for each swarm are chosen from the set of all previously discovered conformations based on a reward function. This function balances (1) preferentially simulating structures with maximum pair-wise distances (Fig. 2A) to encourage the Ω-loop to adapt a more open conformation that may harbor cryptic pockets; with (2) a broad exploration of conformational space. The pair-wise distances were chosen from the residues located at the beta strands of ECD to the same at the Ω-loop, resulting in a total of 125 pairs, 25 per monomer. The broad exploration phase was implemented by favoring states that are poorly sampled compared to other states, based on the root root-mean-square deviation of the ECD residues. During FAST, we performed 30 generations of simulations with 25 simulations/generation and 40 ns/simulation, totaling 30 μs. Since no biasing force is applied to any individual simulation, the final

data set can be used to build a Markov state model (MSM) to extract the proper thermodynamics and kinetics [47–49], as detailed below.

Markov state modeling

We used our trajectory dataset from FAST to construct a Markov state model (MSM) using pyEmma [50], by first featurizing the trajectory dataset using the 125 residue-residue distance pairs used for FAST sampling, as described above. The conformational space was then discretized into 1000 microstates using k-means clustering. Then, a transition probability matrix (TPM) was constructed by evaluating the probability of transitioning between each microstate within a lag time, τ. To choose an adequate lag time to construct a TPM that ensures Markovian behavior, multiple TPMs were first created using multiple maximum-likelihood MSMs with different lag times. The implied timescales were evaluated for each of these transition matrices, and saturation was observed at $\tau = 5\,\text{ns}$ (Fig. S6). Thus, we built our final TPM using a maximum likelihood MSM with a lag time of 5 ns. This final TPM is symmetrized using a maximum likelihood approach to ensure detailed balance [50].

MD simulations

MD simulations in this study were performed using GROMACS-2023 [51] utilizing CHARMM36m [25] and CHARMM36 [52] force field parameters for proteins and lipids, respectively. The force field parameters for the ligands were generated using the CHARMM General Force Field (CGenFF) [26–28]. Cation-π interaction-specific NBFIX parameters were used to maintain appropriate ligand-protein interactions at the aromatic cage, located at the binding sites [53]. Bonded and short-range non-bonded interactions were calculated every 2 fs, and periodic boundary conditions were employed in all three dimensions. The particle mesh Ewald (PME) method [54] was used to calculate long-range electrostatic interactions with a grid spacing below 0.1 nm^{-3}. A force-based smoothing function was employed for pairwise nonbonded interactions at 1 nm with a cutoff of 1.2 nm. Pairs of atoms whose interactions were evaluated were searched and updated every 20 steps. A cutoff of 1.2 nm was applied to search for the interacting atom pairs. Constant pressure was maintained at 1 bar using the Parrinello-Rahman barostat [55] and temperature was kept at 300K with the v-rescale thermostat [56].

Molecular docking

All the FAST sampled conformations were used for molecular docking of 4-bromoamphetamine using AutoDock Vina [57]. A grid box of dimensions of 24 x 22 x 25 Å^3 at the vestibular site was employed for docking, outputting the best docking scored pose for each protein conformation.

Analysis

System visualization and analysis were carried out using VMD and PyMOL [46, 58]. The "measure cluster" module implemented in VMD [59] was used for clustering analysis.

Expression in oocytes and electrophysiology

The gene encoding mouse 5-HT_{3A}R was inserted into the pBK-CMV expression vector. The desired mutation was created by site-directed mutagenesis using the Phusion High–Fidelity DNA Polymerase (ThermoFisher). The PCR product was digested overnight with DpnI at 37 °C and transformed into XL1-Blue Supercompetent cells (Agilent) and the mutation was confirmed by sequencing (Eurofins Genomics). Oocytes from female Xenopus laevis frogs (Ecocyte Bioscience) were injected into the animal pole with 6 ng/32.2 nl DNA and incubated for 3–9 days at 13°C in MBS (88 mM NaCl, 1 mM KCl, 2.4 mM $NaHCO_3$, 0.91 mM $CaCl_2$, 0.82 mM $MgSO_4$, 0.33 mM $Ca(NO_3)_2$, 10 mM HEPES, 0.5 mM theophylline, 0.1 mM G418, 17 mM streptomycin, 10,000 U/l penicillin and 2 mM sodium pyruvate, adjusted to pH 7.5) before two-electrode voltage-clamp (TEVC) recordings.

For TEVC recordings, glass electrodes filled with 3 M KCl (5 - 50 MΩ) were used to voltage-clamp the oocyte membrane potential at -70 mV with an OC-725C voltage clamp (Warner Instruments). Oocytes were continuously perfused with running buffer (123 mM NaCl, 2 mM KCl, and 2 mM $MgSO_4$, and adjusted to pH 7.5) at a flow rate of 20 rpm. Currents were sampled and digitized at a sampling rate of 1 kHz with a Digidata 1440A. Current traces were plotted and analyzed by Clampfit (Molecular Devices).

For each BrAmp recording occasion, 1M stock solution of BrAmp dissolved in DMSO was prepared. The wash period between each 30-sec application was 10 min. After each BrAmp-containing application, the two upcoming applications were solely running buffer with $\sim$ EC20 5-HT to guarantee re-sensitization. Dose-response curves were fitted by nonlinear regression to the Boltzmann equation with variable slope and amplitudes using Prism 10.0.3 (GraphPad Software). Each reported value represents the mean $\pm$ SEM for n $\geq$ four oocytes, and is analyzed with unpaired t-tests, with significant effects set at $P < 0.05$.

Acknowledgments. We thank Maxwell Zimmerman for his valuable feedback and discussion on the FAST simulation setup and troubleshooting. MD simulations were performed using computing facilities of the Karolina, LUMI and Discoverer Supercomputer through EuroHPC (grant nos. EHPC-REG-2023R01-103, EHPC-REG-2022R03-223 and EHPC-REG-2022R03-219, respectively) and the Swedish National Infrastructure for Computing (SNIC 2022/3-40) and supported by BioExcel (EuroHPC grant no. 101093290). N.H. was supported by a Marie Sklodowska-Curie Postdoctoral Fellowship (grant no. 101107036), E.K. by a Sven & Lily Lawski Foundation Doctoral Fellowship, and R.J.H., and E.L. by grants from the Swedish Research Council (2019-02433, 2021-05806) and Swedish e-Science Research Center.

Data and code availability. The raw MD simulation trajectories can be found at Zenodo: 10.5281/zenodo.10812994.

Author contributions. N.H. designed research, performed the simulations and analyzed data; E.K. designed research, performed the experiments and analyzed data; and N.H., E.K., R.J.H., and E.L. wrote the paper. All authors read and contributed to finalizing the paper.

Declaration of interests. The authors declare no competing interests.

References

[1] Lester, H.A., Dibas, M.I., Dahan, D.S., Leite, J.F., Dougherty, D.A.: Cys-loop receptors: new twists and turns. Trends in neurosciences **27**(6), 329–336 (2004)

[2] Lynagh, T., Pless, S.A.: Principles of agonist recognition in Cys-loop receptors. Frontiers in physiology **5**, 160 (2014)

[3] Zarkadas, E., Zhang, H., Cai, W., Effantin, G., Perot, J., Neyton, J., Chipot, C., Schoehn, G., Dehez, F., Nury, H.: The binding of palonosetron and other antiemetic drugs to the serotonin 5-HT3 receptor. Structure **28**(10), 1131–1140 (2020)

[4] Sigel, E., Ernst, M.: The benzodiazepine binding sites of $GABA_A$ receptors. Trends in pharmacological sciences **39**(7), 659–671 (2018)

[5] Sieghart, W., Savić, M.M.: International union of basic and clinical pharmacology. CVI: $GABA_A$ receptor subtype-and function-selective ligands: key issues in translation to humans. Pharmacological reviews **70**(4), 836–878 (2018)

[6] Kim, J.J., Gharpure, A., Teng, J., Zhuang, Y., Howard, R.J., Zhu, S., Noviello, C.M., Walsh Jr, R.M., Lindahl, E., Hibbs, R.E.: Shared structural mechanisms of general anaesthetics and benzodiazepines. Nature **585**(7824), 303–308 (2020)

[7] Spurny, R., Ramerstorfer, J., Price, K., Brams, M., Ernst, M., Nury, H., Verheij, M., Legrand, P., Bertrand, D., Bertrand, S., Dougherty, D.A., Esch, I.J.P., Corringer, P.-J., Sieghart, W., Lummis, S.C.R., Ulens, C.: Pentameric ligand-gated

ion channel ELIC is activated by GABA and modulated by benzodiazepines. Proceedings of the National Academy of Sciences **109**(44), 3028–3034 (2012)

[8] Van Renterghem, C., Nemecz, Á., Delarue-Cochin, S., Joseph, D., Corringer, P.-J.: Fumarate as positive modulator of allosteric transitions in the pentameric ligand-gated ion channel GLIC: Requirement of an intact vestibular pocket. The Journal of Physiology **601**(12), 2447–2472 (2023)

[9] Fourati, Z., Sauguet, L., Delarue, M.: Structural evidence for the binding of monocarboxylates and dicarboxylates at pharmacologically relevant extracellular sites of a pentameric ligand-gated ion channel. Acta Crystallographica Section D: Structural Biology **76**(7), 668–675 (2020)

[10] Renterghem, C.V., Nemecz, A., Madjebeur, K., Corringer, P.-J.: Short-chain mono-carboxylates as negative modulators of allosteric transitions in glic, and impact of a pre-β5 strand (loop ω) double mutation on crotonate, not butyrate effect. Physiol Rep. **12**, 15916 (2024)

[11] Hu, H., Nemecz, Á., Van Renterghem, C., Fourati, Z., Sauguet, L., Corringer, P.-J., Delarue, M.: Crystal structures of a pentameric ion channel gated by alkaline pH show a widely open pore and identify a cavity for modulation. Proceedings of the National Academy of Sciences **115**(17) (2018)

[12] Brams, M., Govaerts, C., Kambara, K., Price, K.L., Spurny, R., Gharpure, A., Pardon, E., Evans, G.L., Bertrand, D., Lummis, S.C., Hibbs, R.E., Steyaert, J., Ulens, C.: Modulation of the *Erwinia* ligand-gated ion channel (ELIC) and the 5-HT_3 receptor via a common vestibule site. Elife **9**, 51511 (2020)

[13] Morales-Perez, C.L., Noviello, C.M., Hibbs, R.E.: X-ray structure of the human $\alpha4\beta2$ nicotinic receptor. Nature **538**(7625), 411–415 (2016)

[14] Walsh Jr, R.M., Roh, S.-H., Gharpure, A., Morales-Perez, C.L., Teng, J., Hibbs, R.E.: Structural principles of distinct assemblies of the human $\alpha4\beta2$ nicotinic receptor. Nature **557**(7704), 261–265 (2018)

[15] Du, J., Lü, W., Wu, S., Cheng, Y., Gouaux, E.: Glycine receptor mechanism elucidated by electron cryo-microscopy. Nature **526**(7572), 224–229 (2015)

[16] Hassaine, G., Deluz, C., Grasso, L., Wyss, R., Tol, M.B., Hovius, R., Graff, A., Stahlberg, H., Tomizaki, T., Desmyter, A., Moreau, C., Li, X.-D., Poitevin, F., Vogel, H., Nury, H.: X-ray structure of the mouse serotonin 5-HT_3 receptor. Nature **512**(7514), 276–281 (2014)

[17] Oleinikovas, V., Saladino, G., Cossins, B.P., Gervasio, F.L.: Understanding cryptic pocket formation in protein targets by enhanced sampling simulations. Journal of the American Chemical Society **138**(43), 14257–14263 (2016)

[18] Meller, A., Ward, M.D., Borowsky, J.H., Lotthammer, J.M., Kshirsagar, M., Oviedo, F., Ferres, J.L., Bowman, G.: Predicting the locations of cryptic pockets from single protein structures using the PocketMiner graph neural network. Biophysical Journal **122**(3), 445 (2023)

[19] Meller, A., Bhakat, S., Solieva, S., Bowman, G.R.: Accelerating cryptic pocket discovery using AlphaFold. Journal of Chemical Theory and Computation **19**(14), 4355–4363 (2023)

[20] Kuzmanic, A., Bowman, G.R., Juarez-Jimenez, J., Michel, J., Gervasio, F.L.: Investigating cryptic binding sites by molecular dynamics simulations. Accounts of chemical research **53**(3), 654–661 (2020)

[21] Zimmerman, M.I., Bowman, G.R.: FAST conformational searches by balancing exploration/exploitation trade-offs. Journal of chemical theory and computation **11**(12), 5747–5757 (2015)

[22] Le Guilloux, V., Schmidtke, P., Tuffery, P.: Fpocket: an open source platform for ligand pocket detection. BMC bioinformatics **10**(1), 1–11 (2009)

[23] Basak, S., Gicheru, Y., Rao, S., Sansom, M.S., Chakrapani, S.: Cryo-EM reveals two distinct serotonin-bound conformations of full-length 5-HT_{3A} receptor. Nature **563**(7730), 270–274 (2018)

[24] Hart, K.M., Ho, C.M., Dutta, S., Gross, M.L., Bowman, G.R.: Modelling proteins' hidden conformations to predict antibiotic resistance. Nature communications **7**(1), 12965 (2016)

[25] Huang, J., Rauscher, S., Nawrocki, G., Ran, T., Feig, M., De Groot, B.L., Grubmüller, H., MacKerell Jr, A.D.: CHARMM36m: an improved force field for folded and intrinsically disordered proteins. Nature methods **14**(1), 71–73 (2017)

[26] Vanommeslaeghe, K., Raman, E.P., MacKerell Jr, A.D.: Automation of the CHARMM general force field (CGenFF) II: assignment of bonded parameters and partial atomic charges. Journal of chemical information and modeling **52**(12), 3155–3168 (2012)

[27] Vanommeslaeghe, K., Hatcher, E., Acharya, C., Kundu, S., Zhong, S., Shim, J., Darian, E., Guvench, O., Lopes, P., Vorobyov, I., Mackerell Jr, A.D.: CHARMM general force field: A force field for drug-like molecules compatible with the CHARMM all-atom additive biological force fields. Journal of computational chemistry **31**(4), 671–690 (2010)

[28] Vanommeslaeghe, K., MacKerell Jr, A.D.: Automation of the CHARMM general force field (CGenFF) I: bond perception and atom typing. Journal of chemical information and modeling **52**(12), 3144–3154 (2012)

[29] Tian, C., Kasavajhala, K., Belfon, K.A., Raguette, L., Huang, H., Migues, A.N., Bickel, J., Wang, Y., Pincay, J., Wu, Q., Simmerling, C.: ff19SB: Amino-acid-specific protein backbone parameters trained against quantum mechanics energy surfaces in solution. Journal of chemical theory and computation **16**(1), 528–552 (2019)

[30] He, X., Man, V.H., Yang, W., Lee, T.-S., Wang, J.: A fast and high-quality charge model for the next generation general AMBER force field. The Journal of Chemical Physics **153**(11) (2020)

[31] Chovancova, E., Pavelka, A., Benes, P., Strnad, O., Brezovsky, J., Kozlikova, B., Gora, A., Sustr, V., Klvana, M., Medek, P., Biedermannova, L., Sochor, J., Damborsky, J.: CAVER 3.0: a tool for the analysis of transport pathways in dynamic protein structures. PLoS Computational Biology **8**(10), 1002708 (2012)

[32] Polovinkin, L., Hassaine, G., Perot, J., Neumann, E., Jensen, A.A., Lefebvre, S.N., Corringer, P.-J., Neyton, J., Chipot, C., Dehez, F., Schoehn, G., Nury, H.: Conformational transitions of the serotonin 5-HT_3 receptor. Nature **563**(7730), 275–279 (2018). Nature Publishing Group UK London

[33] Howard, R.J.: Elephants in the dark: Insights and incongruities in pentameric ligand-gated ion channel models. Journal of Molecular Biology **433**(17), 167128 (2021)

[34] Jumper, J., Evans, R., Pritzel, A., Green, T., Figurnov, M., Ronneberger, O., Tunyasuvunakool, K., Bates, R., Žídek, A., Potapenko, A., Bridgland, A., Meyer, C., Kohl, S.A.A., Ballard, A.J., Cowie, A., Romera-Paredes, B., Nikolov, S., Jain, R., Adler, J., Back, T., Petersen, S., Reiman, D., Clancy, E., Zielinski, M., Steinegger, M., Pacholska, M., Berghammer, T., Bodenstein, S., Silver, D., Vinyals, O., Senior, A.W., Kavukcuoglu, K., Kohli, P., Hassabis, D.: Highly accurate protein structure prediction with AlphaFold. Nature **596**(7873), 583–589 (2021)

[35] Cruz, M.A., Frederick, T.E., Mallimadugula, U.L., Singh, S., Vithani, N., Zimmerman, M.I., Porter, J.R., Moeder, K.E., Amarasinghe, G.K., Bowman, G.R.: A cryptic pocket in ebola VP35 allosterically controls RNA binding. Nature Communications **13**(2269) (2022)

[36] Zimmerman, M., Porter, J., Ward, M., Singh, S., Vithani, N., Meller, A., Mallimadugula, U., Kuhn, C., Borowsky, J., Wiewiora, R., Hurley, M., Harbison, A., Fogarty, C., Coffland, J., Fadda, E., Voelz, V., Chodera, J., Bowman, G.: SARS-CoV-2 simulations go exascale to predict dramatic spike opening and cryptic pockets across the proteome. Nature Chemistry **13**, 651–659 (2021)

[37] Behring, J.B., Post, S., Mooradian, A.D., Egan, M.J., Zimmerman, M.I., Clements, J.L., Bowman, G.R., Held, J.M.: Spatial and temporal alterations in protein structure by EGF regulate cryptic cysteine oxidation. Science signaling **13**(615), 7315 (2020)

[38] Heal, D.J., Smith, S.L., Gosden, J., Nutt, D.J.: Amphetamine, past and present – a pharmacological and clinical perspective. Journal of psychopharmacology **27**(6), 479–496 (2013)

[39] Dean, B.V., Stellpflug, S.J., Burnett, A.M., Engebretsen, K.M.: 2c or not 2c: phenethylamine designer drug review. Journal of Medical Toxicology **9**, 172–178 (2013)

[40] Dämgen, M.A., Biggin, P.C.: A refined open state of the glycine receptor obtained via molecular dynamics simulations. Structure **28**(1), 130–139 (2020)

[41] Jing, Z., Liu, C., Cheng, S.Y., Qi, R., Walker, B.D., Piquemal, J.-P., Ren, P.: Polarizable force fields for biomolecular simulations: Recent advances and applications. Annual Review of biophysics **48**, 371–394 (2019)

[42] Ingólfsson, H.I., Carpenter, T.S., Bhatia, H., Bremer, P.-T., Marrink, S.J., Lightstone, F.C.: Computational lipidomics of the neuronal plasma membrane. Biophysical journal **113**(10), 2271–2280 (2017)

[43] Jo, S., Kim, T., Iyer, V.G., Im, W.: CHARMM-GUI: a web-based graphical user interface for CHARMM. Journal of computational chemistry **29**(11), 1859–1865 (2008)

[44] Jorgensen, W.L., Chandrasekhar, J., Madura, J.D., Impey, R.W., Klein, M.L.: Comparison of simple potential functions for simulating liquid water. The Journal of chemical physics **79**(2), 926–935 (1983)

[45] Licari, G., Dehghani-Ghahnaviyeh, S., Tajkhorshid, E.: Membrane mixer: a toolkit for efficient shuffling of lipids in heterogeneous biological membranes. Journal of Chemical Information and Modeling **62**(4), 986–996 (2022)

[46] Humphrey, W., Dalke, A., Schulten, K.: VMD: visual molecular dynamics. Journal of molecular graphics **14**(1), 33–38 (1996)

[47] Huang, X., Bowman, G.R., Bacallado, S., Pande, V.S.: Rapid equilibrium sampling initiated from nonequilibrium data. Proceedings of the National Academy of Sciences **106**(47), 19765–19769 (2009)

[48] Bowman, G.R., Pande, V.S., Noé, F.: An introduction to markov state models and their application to long timescale molecular simulation. Springer Science & Business Media **797** (2013)

[49] Noé, F., Schütte, C., Vanden-Eijnden, E., Reich, L., Weikl, T.R.: Constructing the equilibrium ensemble of folding pathways from short off-equilibrium simulations. Proceedings of the National Academy of Sciences **106**(45), 19011–19016 (2009)

[50] Scherer, M.K., Trendelkamp-Schroer, B., Paul, F., Pérez-Hernández, G., Hoffmann, M., Plattner, N., Wehmeyer, C., Prinz, J.-H., Noé, F.: PyEMMA 2: A software package for estimation, validation, and analysis of Markov models. Journal of chemical theory and computation **11**(11), 5525–5542 (2015)

[51] Páll, S., Zhmurov, A., Bauer, P., Abraham, M., Lundborg, M., Gray, A., Hess, B., Lindahl, E.: Heterogeneous parallelization and acceleration of molecular dynamics simulations in GROMACS. The Journal of Chemical Physics **153**(13), 134110 (2020)

[52] Klauda, J.B., Venable, R.M., Freites, J.A., O'Connor, J.W., Tobias, D.J., Mondragon-Ramirez, C., Vorobyov, I., MacKerell Jr, A.D., Pastor, R.W.: Update of the CHARMM all-atom additive force field for lipids: validation on six lipid types. The journal of physical chemistry B **114**(23), 7830–7843 (2010)

[53] Liu, H., Fu, H., Chipot, C., Shao, X., Cai, W.: Accuracy of alternate nonpolarizable force fields for the determination of protein-ligand binding affinities dominated by cation- π interactions. Journal of Chemical Theory and Computation **17**(7), 3908–3915 (2021)

[54] Darden, T., York, D., Pedersen, L.: Particle mesh Ewald: An $N{\cdot}\log(N)$ method for Ewald sums in large systems. The Journal of chemical physics **98**(12), 10089–10092 (1993)

[55] Parrinello, M., Rahman, A.: Crystal structure and pair potentials: A molecular-dynamics study. Physical review letters **45**(14), 1196 (1980)

[56] Bussi, G., Donadio, D., Parrinello, M.: Canonical sampling through velocity rescaling. The Journal of chemical physics **126**(1), 014101 (2007)

[57] Trott, O., Olson, A.J.: Autodock Vina: Improving the speed and accuracy of docking with a new scoring function, efficient optimization, and multithreading. Journal of computational chemistry **31**(2), 455–461 (2010)

[58] DeLano, W.L.: PyMOL: An open-source molecular graphics tool. CCP4 Newsl. Protein Crystallogr **40**(1), 82–92 (2002)

[59] Heyer, L.J., Kruglyak, S., Yooseph, S.: Exploring expression data: identification and analysis of coexpressed genes. Genome research **9**(11), 1106–1115 (1999)

Supplementary Figures and Tables

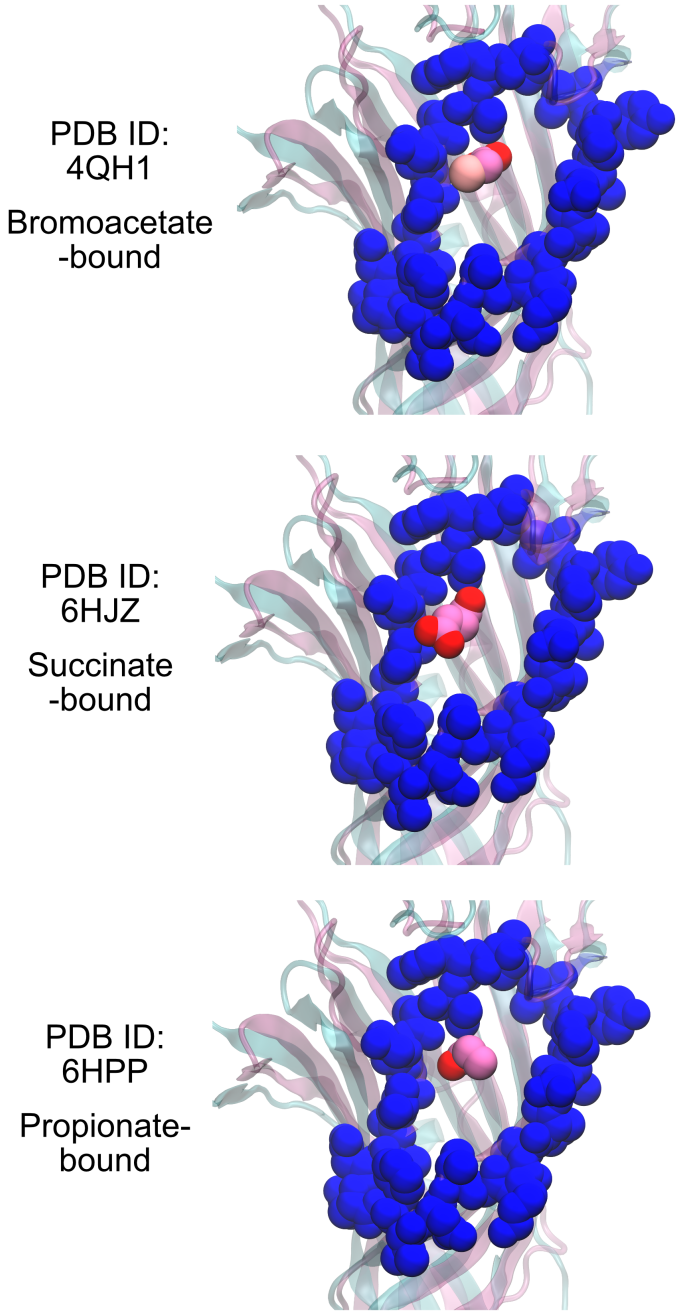

Fig. S1 Structural alignment of putative vestibular sites in GLIC bound to different carboxylates (pink) and the 5-HT_{3A}R (PDB ID: 6DG8, blue). In GLIC, spheres represent vestibule-bound ligands and in the 5-HT_{3A}R, spheres represent amino-acid side chains in the Ω-loop.

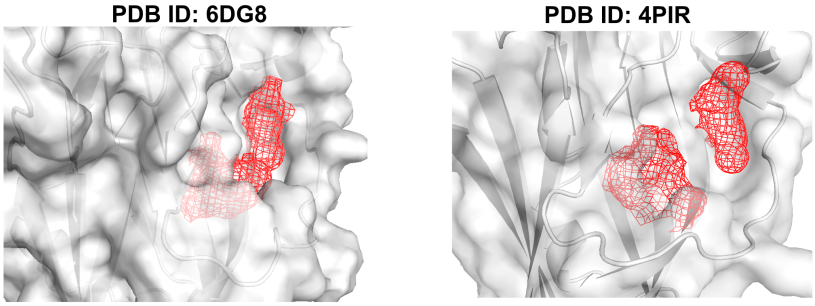

Fig. S2 Pocket volumes at the 5-HT_{3A}R vestibular site, generated in Fpocket [22], show no clear cavity for drug binding in two different activated experimental structures.

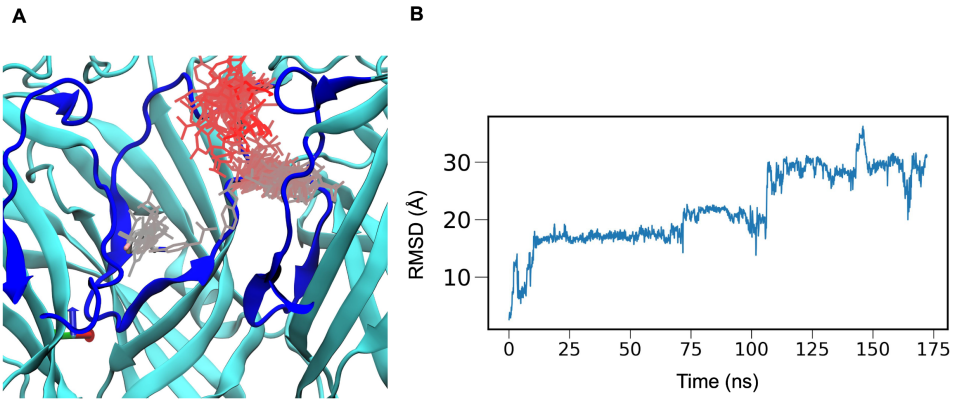

Fig. S3 A) Docking of 4-bromoamphetamine to an activated-state 5-HT_{3A}R (PDB ID: 6DG8) [23] did not produce stable binding, as illustrated by the time evolution of the ligand during simulation, colored by frame (white to red). B) RMSD of the ligand with respect to its original docked position during MD simulation.

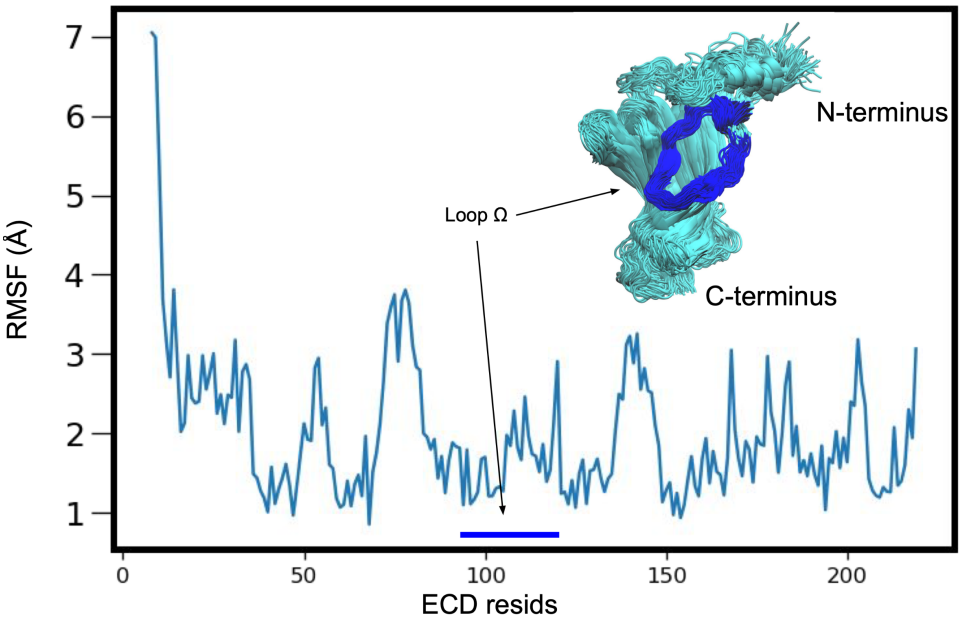

Fig. S4 Root-mean-square fluctuation (RMSF) of ECD residues over the first generation of FAST simulations (25 replicates, 1 μs total simulation time). Inset shows sampled ECD conformations as cyan ribbons, with the Ω-loop in blue.

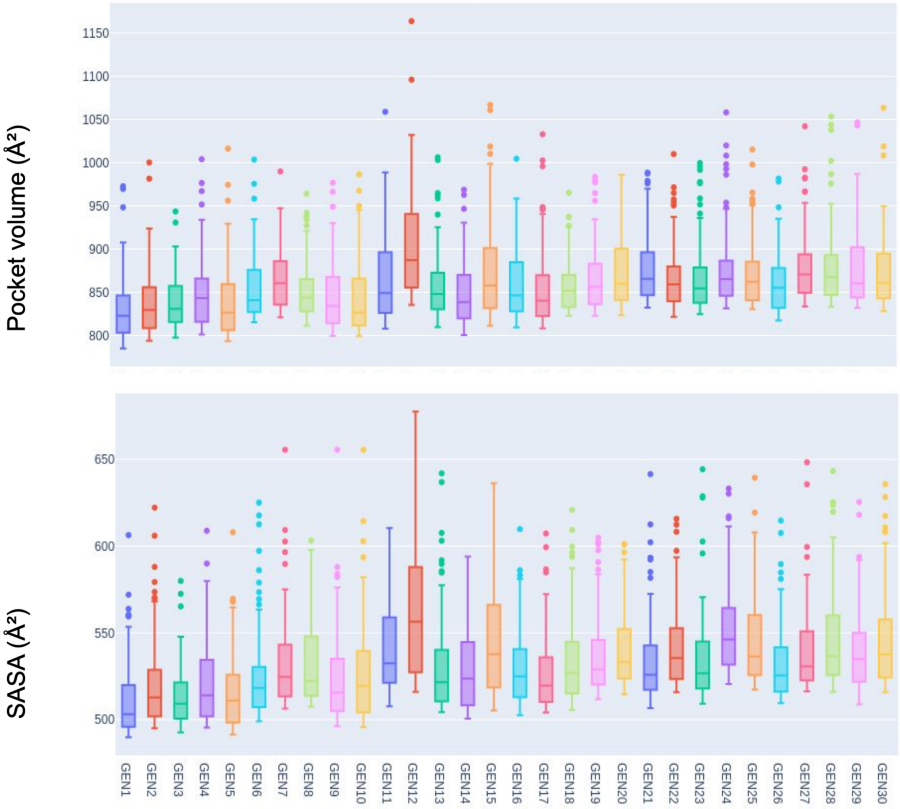

Fig. S5 Box plot of pocket volumes and solvent-exposed surface areas in at the vestibular site, calculated using CAVER [31] for each FAST generation. Calculations were done with the highest 100 values for each generation.

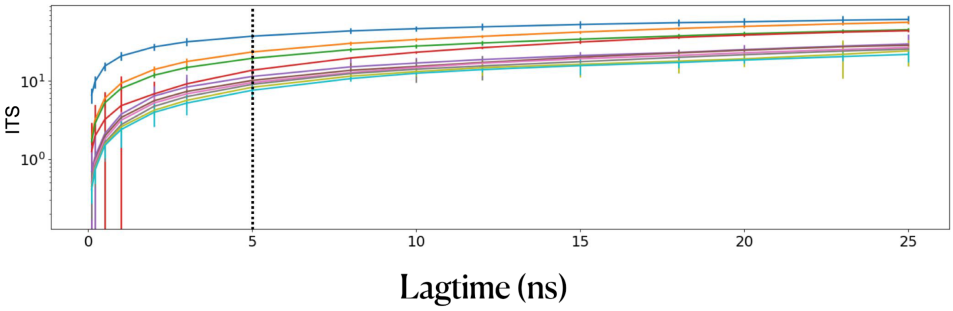

Fig. S6 Implied timescales (ITS) plot of the top 10 slowest processes using multiple lag times in Markov state modeling of FAST sampling trajectories. Error bars indicate the uncertainty evaluated using a Bayesian estimated Markov state model. A lag time of 5 ns (dotted line) was chosen for Markov state model construction.

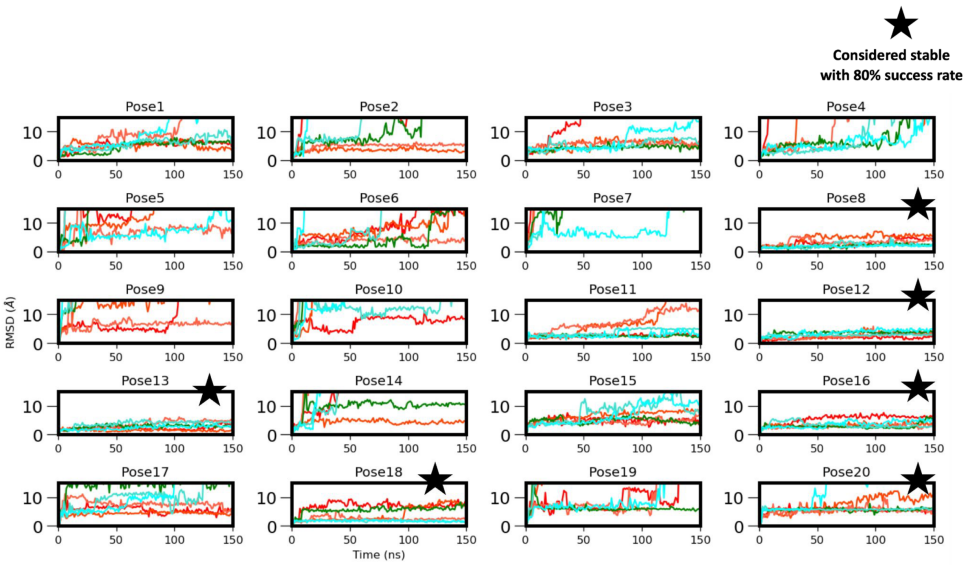

Fig. S7 RMSD of 4-bromoamphetamine from its initial docked pose during MD simulations of each system simulated in three replicates each in CHARMM36 (shades of blue) and AMBER (shades of red). Stars indicate systems selected for further analysis due to remaining within 15 Å RMSD throughout at least 5 of 6 replicates,

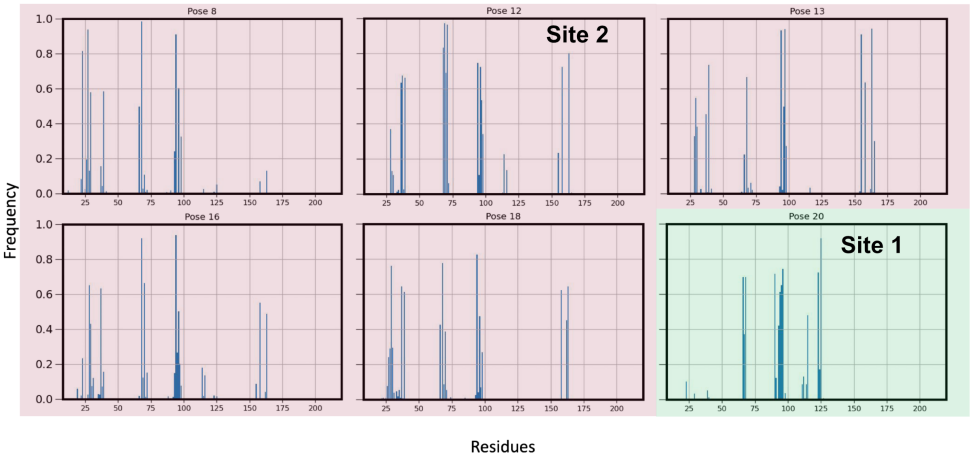

Fig. S8 Frequency of contacts of 4-bromoamphetamine to individual residues of the 5-$HT_{3A}R$ in stable MD simulations of selected poses (Fig. S7). A contact is counted if two atoms of the ligand and receptor are within 4 $\AA$. Green and red shading indicate categorization as sites 1 and 2, respectively, based on patterns of contacting residues.

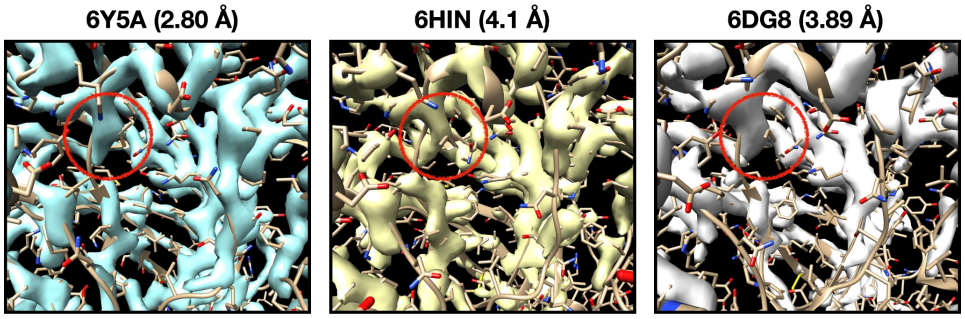

Fig. S9 Cryo-EM densities and corresponding models for activated structures of the 5-HT$_{3A}$R. Red circles highlight the densities around residue V95.